Spreading dynamics of polymer nanodroplets in cylindrical geometries

David R. Heine, Gary S. Grest, and Edmund B. Webb III
Sandia National Laboratories, Albuquerque, New Mexico 87185, USA
(Received 2 April 2004; published 27 July 2004)

The spreading of one- and two-component polymer nanodroplets is studied using molecular dynamics simulation in a cylindrical geometry. The droplets consist of polymer chains of length 10, 40, and 100 monomers per chain described by the bead-spring model spreading on a flat surface with a surface-coupled Langevin thermostat. Each droplet contains ~350 000 monomers. The dynamics of the individual components of each droplet is analyzed and compared to the dynamics of single-component droplets for the spreading rates of the precursor foot and bulk droplet, the time evolution of the contact angle, and the velocity distribution inside the droplet. We derive spreading models for the cylindrical geometry analogous to the kinetic and hydrodynamic models previously developed for the spherical geometry, and show that hydrodynamic behavior is observed at earlier times for the cylindrical geometry. The contact radius is predicted to scale as $r(t) \sim t^{1/5}$ from the kinetic model and $r(t) \sim t^{1/7}$ for the hydrodynamic model in the cylindrical geometry.

DOI: 10.1103/PhysRevE.70.011606 PACS number(s): 68.47.Pe

I. INTRODUCTION

Practical applications of the spreading of a liquid on a solid are prevalent in the lubrication, coatings, and printing industries, to name a few. Knowledge of the rates of spreading and equilibrium configurations of these systems is crucial for improving their performance. Extensive experimental, theoretical, and computational work has been undertaken to better understand the interaction between a liquid and solid in contact. Most frequently, the liquids studied are oligomers or polymers in order to remove the influence of evaporation and condensation on the droplet spreading dynamics.

The total energy dissipation in a spreading droplet can be represented as a sum of three different components: one due to the hydrodynamic flow in the bulk of the droplet, one due to the viscous dissipation in the precursor foot, and one due to the adsorption and desorption of molecules to the solid surface in the vicinity of the contact line [1]. Experimental measurements [2,3] of microscopic droplets compare well with the hydrodynamic model of droplet spreading [4–7], indicating that hydrodynamic energy dissipation is an important feature of droplet spreading. To date, however, simulations [8–16] of spherical droplets have been unable to approach the droplet size and time duration required for hydrodynamic flow to be relevant.

Although simulations of spreading droplets typically consider a three-dimensional spreading hemisphere, there are computational advantages for considering a two-dimensional hemicylinder [17,18]. The symmetry along the cylinder axis allows periodic boundary conditions to be applied in one direction, and a larger droplet radius r can be simulated with fewer atoms since the droplet volume scales as r^2 in the cylindrical geometry instead of r^3 for the spherical geometry. With larger droplet sizes, this enables us to simulate more viscous systems by including polymer chains of length $N = 100$ in droplet spreading simulations.

It has been claimed that hydrodynamic dissipation is dominant for small contact angles and nonhydrodynamic dissipation is dominant for relatively large contact angles [19]. This is reinforced by the fact that for spherical droplets, spreading models have a kinetic dissipation term that is linear in the instantaneous contact radius, while the hydrodynamic dissipation term has a logarithmic dependence on the instantaneous contact radius [2,3,20]. We show here that for a cylindrical geometry, the hydrodynamic dissipation term is linearly dependent on the contact radius, which suggests that hydrodynamic flow could contribute to the dissipation at earlier times for a cylindrical geometry than for the spherical geometry. Our simulations show that this is indeed the case. We also show that the $r(t) \sim t^{1/10}$ scaling of Tanner's spreading law and the $r(t) \sim t^{1/7}$ prediction of molecular-kinetic theory for spherical droplets become $r(t) \sim t^{1/7}$ and $r(t) \sim t^{1/5}$, respectively, in the cylindrical geometry.

Even though many of the liquids used in surface wetting applications are mixtures or suspensions, most of the research has focused on single-component liquids. Some experimental [21–24] and theoretical [25,26] work has been done on binary droplets focusing mainly on the equilibrium behavior. Simulations of binary droplets containing from 4 000 [27–30] to 25 000 [31] monomers have been performed, but larger system sizes are needed to adequately model the spreading dynamics.

In this paper, we present molecular dynamics (MD) simulations of coarse-grained models of one- and two-component polymer droplets for chain length $N = 10$, 40, and 100. These chain lengths are chosen since they have a very low vapor pressure and the droplet spreading is not influenced by vaporization and condensation. We analyze the dynamics of the components of each droplet and compare the spreading rates of two-component droplets to their single-component analogs. We derive the equations for the rate of change of contact angle and radius for the cylindrical geometry based on kinetic [32–34] and hydrodynamic models [3,4,35], and we use these models to extract physical parameters for each system.

The paper is organized as follows. Section II describes the details of the molecular dynamics simulations and the application of the Langevin thermostat to the monomers near the substrate. It also describes the methods used to analyze the simulation results. Section III presents the droplet spreading models for the cylindrical geometry. Section IV compares the spreading behavior of monodispersed droplets in the

spherical and cylindrical geometry, droplets of different chain lengths, and binary mixtures. The velocity distributions of both homogeneous and binary droplets are analyzed in Sec. V and conclusions are presented in Sec. VI.

II. SIMULATION DETAILS

A. Potentials and thermostat

Molecular dynamics (MD) simulations are performed using a coarse-grained model for the polymer chains in which the polymer is represented by spherical beads of mass m attached by springs. We use a truncated Lennard-Jones (LJ) potential to describe the interaction between the monomers. The LJ potential is given by

$$U_{LJ}(R) = \begin{cases} 4\varepsilon\left[\left(\frac{\sigma}{r}\right)^{12} - \left(\frac{\sigma}{r}\right)^{6}\right] & r \leqslant r_c \\ 0 & r > r_c, \end{cases} \quad (1)$$

where ε and σ are the LJ units of energy and length and the cutoff is set to $r_c = 2.5\ \sigma$. The monomer-monomer interaction ε is used as the reference and all monomers have the same diameter σ. Although in this paper for the binary mixtures we vary only the chain length, in future work we will vary the relative interaction strength. For bonded monomers, we apply an additional potential where each bond is described by the finite extensible nonlinear elastic (FENE) potential [36] with $k = 30\ \varepsilon$ and $R_0 = 1.5\ \sigma$.

Droplets composed of polymer chains of length N = 10, 40, 100, or 10/40 and 10/100 mixtures of equal mole fraction of monomers are generated by equilibrating a melt of the polymer containing 500 000 monomers at $P \simeq 0$ between two parallel plates in the z direction with periodic boundary conditions in the other two directions. The distance between the plates $L_z \simeq 90\ \sigma$. For the cylindrical geometry, the width of the simulation cell in the y direction is chosen to be wide enough such that there are no interactions between a chain and its periodic image. The larger the width, the better the statistical averaging of contact angle and radius measurements of the droplets. We found that both $L_y = 40$ and $60\ \sigma$ give results with reasonable uncertainty in these measurements. For the spherical droplet, the dimensions $L_x = L_y$. The cylindrical droplets were constructed by removing all chains with centers outside of a hemicylinder of radius $R_0 = 80\ \sigma$ in the xz plane and $L_y = 40\ \sigma$, which resulted in droplets containing $\sim$350 000 monomers. For $R_0 = 50\ \sigma$ and $L_y = 60\ \sigma$, the droplets contained $\sim$200 000 monomers. Hemispherical droplets were constructed in a similar manner, with initial radii $\sim 48\ \sigma$, resulting in a droplet also of $\sim$200 000 monomers. The droplets were then placed above a substrate which initially has an interaction strength chosen so that the droplet equilibrates with a contact angle near 90°. This is necessary since the method of construction of the drop leaves some segments extending into the vapor phase. These dangling chain segments quickly coalesce with the droplet after a short equilibration run. Hemispheres and hemicylinders were chosen over spheres and cylinders to avoid the substantial simulation time required for the isotropic droplet to transition to a cap geometry [8]. All of the droplets studied here are large enough to avoid the equilibrium contact angle dependence on droplet size observed for smaller system sizes [8].

The substrate is modeled as a flat surface with interactions between the surface and the monomers in the droplet at a distance z from the surface modeled using the integrated LJ potential with the cutoff set to $z_c = 2.2\ \sigma$. It was found previously [8] that with the proper choice of thermostat, the simulations using a flat surface exhibit the same behavior as a realistic atomic substrate with greater computational efficiency.

We apply the Langevin thermostat using the same approach as in our earlier paper [8] to provide a realistic representation of the transfer of energy in the droplet. The Langevin thermostat simulates a heat bath by adding Gaussian white-noise and friction terms to the equation of motion

$$m_i \ddot{\mathbf{r}}_i = -\mathbf{\Delta} U_i - m_i \gamma_L \mathbf{r}_i + \mathbf{W}_i(t), \quad (2)$$

where m_i is the mass of monomer i, γ_L is the friction parameter for the Langevin thermostat, $-\mathbf{\Delta} U_i$ is the force acting on monomer i due to the potentials defined above, and $\mathbf{W}_i(t)$ is a Gaussian white-noise term. Coupling all of the monomers to the Langevin thermostat would have the unphysical effect of screening the hydrodynamic interactions in the droplet and not damping the monomers near the surface stronger than those in the bulk. To overcome this, we use a Langevin coupling term with a damping rate that decreases exponentially away from the substrate [37]. We choose the form $\gamma_L(z) = \gamma_L^s \exp(\sigma - z)$, where γ_L^s is the surface Langevin coupling. We generally use values of $\gamma_L^s = 10.0\ \tau^{-1}$ and $3.0\ \tau^{-1}$ for $\varepsilon_w = 2.0\ \varepsilon$ and $3.0\ \varepsilon$, respectively, based on earlier work [8] matching the diffusion constant of the precursor foot for flat and atomistic substrates. The larger γ_L^s corresponds to an atomistic substrate with larger corrugation and hence larger dissipation and slower diffusion near the substrate.

The equations of motion are integrated using a velocity-Verlet algorithm. We use a time step of $\Delta t = 0.01\ \tau$, where $\tau = \sigma(m/\varepsilon)^{1/2}$. The simulations are performed at a temperature $T = \varepsilon / k_B$ using the LAMMPS code [38]. Most of the simulations were run on 64 to 100 processors of Sandia's ICC Intel Xeon cluster. One million steps for a wetting drop of 350 000 monomers takes 24 to 86 h on 64 processors depending on the radius of the droplet.

B. Analysis details

For all of the simulations presented here, we extract the instantaneous contact radius $r(t)$ and contact angle $\theta(t)$ every $400\ \tau$. The contact radius is calculated by defining a one-dimensional radial distribution function, $g(r) = \rho(r)/\rho$, based on every monomer within $1.5\ \sigma$ of the surface, where $\rho(r)$ is the local density at a distance r from the center of mass of the droplet and ρ is the integral of $\rho(r)$ over the entire surface. The contact radius is defined as the distance r at which $g(r) = 0.98$. The same calculation is used to obtain the droplet radius for ten slices of the droplet at incremental heights every $1.5\ \sigma$ from the surface. Fitting a line to the resulting points gives the instantaneous contact angle. For simulations that exhibit a precursor foot, the monomers within $4.5\ \sigma$ of

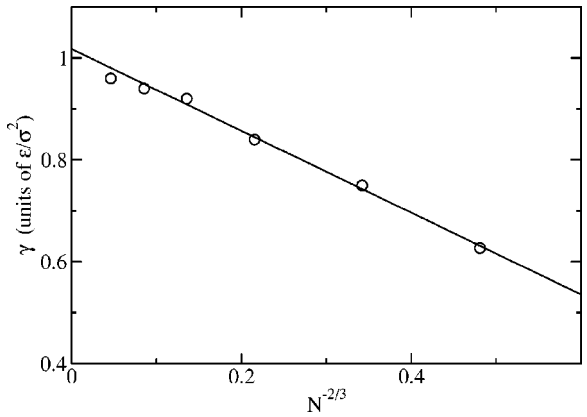

FIG. 1. Molecular weight dependence of the liquid/vapor surface tension for $T=\varepsilon/k_B$. The solid line is a fit to the experimentally observed $N^{-2/3}$ dependence.

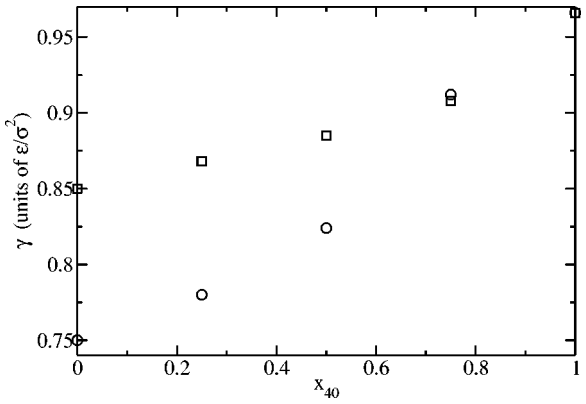

FIG. 2. Surface tension of binary blends of $N=40$ polymers with $N=5$ polymers (○) and $N=10$ polymers (□) as a function of the bulk mole fraction x_{40} of monomers on $N=40$ chains.

the surface are ignored in the contact angle calculation.

Fitting the spreading models to the contact angle and contact radius data requires knowledge of both the surface tension and viscosity. The surface tension is obtained by simulating the polymer melt in a slab geometry so that there are two surfaces perpendicular to the z direction. For $N \geqslant 40$ and all blends, the melt contains 200 000 monomers and each surface has a cross-sectional area of 4900 σ^2. For shorter chain lengths, the melts contain 100 000 monomers and each surface has a cross-sectional area of 2500 σ^2. After the system equilibrates, the surface tension is calculated from the parallel and perpendicular components of the pressure tensor via [39]

$$\gamma = \frac{1}{2}\int_0^{L_z} [p_\perp(z) - p_\parallel(z)]dz. \tag{3}$$

The driving force for the spontaneous spreading of a droplet is the difference in surface tension at each interface. Since the liquid/vapor surface tension γ is dependent on the chain length, the spreading rate is as well. Figure 1 shows a plot of γ for droplets of several chain lengths obtained from MD simulation. The data fit the experimentally [40] observed $N^{-2/3}$ molecular weight dependence very well and provide a means to both extrapolate values of γ for large molecular weights and estimate the change in spreading rate for different chain lengths.

To determine the composition dependence of the surface tension of the binary droplets, we equilibrate blends of $N=40$ with $N=5$ and with $N=10$ at three blend compositions as shown in Fig. 2, and $N=100$ with $N=10$ at a composition $x_{100}=0.5$. This allows us to compare the cases where there is a large (5/40 system) or a moderate difference (10/40 system) in the surface tension of the pure components. Note that the surface tension shown in Fig. 2 is not a simple mean-field (i.e., linear) function of the monomer fraction, as the fully equilibrated surface composition consists of almost fully shorter chains.

The viscosity is calculated from the equilibrium fluctuations of the off-diagonal components of the stress tensor [41] obtained from polymer melt simulations at $T=\varepsilon/k_B$ with the bulk pressure $P \simeq 0$ without tail corrections [8]. We do not include the tail corrections to the pressure in order to match the system of the spreading droplet. These simulations are run up to 84 000 τ. The autocorrelation function of each off-diagonal component of the stress tensor is calculated using the *Numerical Recipes* routine, CORREL [42]. The autocorrelation functions are averaged to improve statistical uncertainty. The results for γ and η are also summarized in Table I.

The viscosity of each blend is obtained in the same manner as the pure components. The surface tension and viscosity for each blend is given in Table II. The surface tensions of the mixtures are closer to that of the shorter chains since they dominate the liquid/vapor interface in the equilibrated system. However, the viscosity of the mixture is more strongly influenced by the longer chains.

III. CYLINDRICAL GEOMETRY DROPLET SPREADING MODELS

The droplet is modeled as a cylindrical cap as shown by the hatched region in Fig. 3. Here, the droplet volume is defined as the cap of height h and width $2r$ of the cylinder with radius R and length L. The cap height can be expressed in terms of the contact angle, θ, as

$$h = r\frac{1-\cos(\theta)}{\sin(\theta)}. \tag{4}$$

Using the definition for the area of a circular segment, $A = \frac{1}{2}R^2(2\theta - \sin 2\theta)$, the radius of the cap can be written in terms of θ and differentiated to give

$$\frac{dr}{dt} = \left(\frac{A}{\theta - \sin\theta\cos\theta}\right)^{1/2}\left(\cos\theta - \frac{\sin^3\theta}{\theta - \sin\theta\cos\theta}\right)\frac{d\theta}{dt}. \tag{5}$$

The free energy is determined by integrating the surface tensions of the liquid/vapor, solid/vapor, and solid/liquid interfaces over the areas of each interface. For the cylindrical cap geometry shown in Fig. 3, this is given by

TABLE I. Bulk properties of bead-spring chains obtained from MD simulation and model fit parameters for $T=\varepsilon/k_B$, $P\simeq 0$. The Lennard-Jones units are given in parenthesis.

						Kinetic	Hydro	Combined				
N	$\varepsilon_w(\varepsilon)$	$\gamma_L^s(\tau^{-1})$	$\rho(\sigma^{-3})$	$\gamma(\varepsilon/\sigma^2)$	$\eta(m/\tau\sigma)$	$\zeta_0(m/\tau\sigma)$	$a(\sigma)$	$\zeta_0(m/\tau\sigma)$	$a(\sigma)$	χ^2_{kin}	χ^2_{hydro}	χ^2_{comb}
10	2.0	10.0	0.869	0.84±0.02	11.1±0.4	72.2	30.3	124	190	.0014	.0049	.0012
10	3.0	3.0	0.869	0.84±0.02	11.1±0.4	37.4	60.4	63.2	147	.0029	.0045	.0012
40	2.0	10.0	0.886	0.94±0.02	41.7±1.4	141	58.2	339	181	.0008	.0066	.0011
40	3.0	3.0	0.886	0.94±0.02	41.7±1.4	59.9	73.6	160	140	.0037	.011	.0018
100	2.0	10.0	0.892	0.96±0.02	132±2	180	41.2	155	51.8	.0015	.0009	.0009
100	3.0	3.0	0.892	0.96±0.02	132±2	82.4	70.7	417	124	.0057	.013	.0019
100	2.0	3.0	0.892	0.96±0.02	132±2	105	65.0	678	155	.0012	.016	.0022
100	3.0	10.0	0.892	0.96±0.02	132±2	167	61.2	126	77.3	.0057	.0005	.0004

$$F\{r(t)\} = 2r(t)L(\gamma_{SL} - \gamma_{SV}) + 2\gamma L\int_0^{r(t)} dx\left[1 + \left(\frac{\partial h'(x,t)}{\partial x}\right)^2\right]^{1/2}, \tag{6}$$

where γ, γ_{SV}, and γ_{SL} are the liquid/vapor, solid/vapor, and solid/liquid surface tensions, respectively. The height of the cylindrical cap in terms of the cap dimensions is given by

$$h'(x,t) = \frac{r(t)}{\sin\,\theta}\left[1 - \left(\frac{x^2\sin^2\,\theta}{r(t)^2}\right)^{-1/2} - \cos\,\theta\right]. \tag{7}$$

Combining Eqs. (6) and (7) and differentiating gives

$$\frac{\partial F\{r(t)\}}{\partial r(t)} = 2L\gamma\left(\frac{\theta}{\sin\,\theta} - \frac{\theta_0}{\sin\,\theta_0}\right). \tag{8}$$

Using the standard mechanical description of dissipative system dynamics, the dissipation function can be represented as

$$\frac{\partial T\{r(t);\dot r(t)\}}{\partial \dot r(t)} = \frac{\partial F\{r(t)\}}{\partial r(t)}, \tag{9}$$

where T is the dissipation function [1,43], which we consider to be composed of a kinetic component $T\dot\Sigma_l$ and a hydrodynamic component $T\dot\Sigma_w$. The kinetic dissipation term, due to molecular adsorption near the contact line, follows the kinetic model introduced by Eyring and co-workers [32] and applied to spreading of a spherical droplet by Blake and Haynes [33,34]. In the kinetic model, the liquid molecules jump between surface sites separated by a distance λ with a frequency K. For the spreading cylinder, the velocity of the contact line to first order is obtained from Eq. (8) as

$$\dot r(t) = \frac{2\gamma}{\zeta_0}\left(\frac{\theta}{\sin\,\theta} - \frac{\theta_0}{\sin\,\theta_0}\right), \tag{10}$$

where the friction coefficient $\zeta_0 \equiv \Delta n k_B T/K\lambda$. Here, Δn is the density of sites on the solid surface. Combining Eqs. (8)–(10), we find that the dissipation term due to the surface kinetics is

$$T\dot\Sigma_l = \zeta_0\dot r(t)^2 L/2. \tag{11}$$

The hydrodynamic dissipation term for the spreading droplet is obtained by solving the equations of motion and continuity. For the spherical droplet, Seaver and Berg [35] found that approximating the spherical cap as a cylindrical disk of the same volume gave results that differed from the rigorous derivation by Cox [4] only by insignificant numerical factors. We apply the same approximation here, treating the hydrodynamics of the cylinder as identical to that of a rectangular box as shown in Fig. 4. Following de Ruijter *et al.* [3], we set the velocity of the upper part of the leading edge to the droplet spreading velocity, $v_x[x=r(t), z=h'] = \dot r(t)$. With this boundary condition, the velocity profile is simply

$$v_x(x,z) = \frac{z}{h'(x,t)}\dot r(t). \tag{12}$$

The hydrodynamic dissipation Σ_w is defined as

$$T\dot\Sigma_w = \eta\int_V dV\left(\frac{\partial v_x}{\partial z}\right)^2. \tag{13}$$

Combining Eqs. (12) and (13) and integrating gives

TABLE II. Bulk properties and model fit parameters for binary droplets. The Lennard-Jones units are given in parentheses.

						Kinetic	Hydro	Combined				
N	$\varepsilon_w(\varepsilon)$	$\gamma_L^s(\tau^{-1})$	$\rho(\sigma^{-3})$	$\gamma(\varepsilon/\sigma^2)$	$\eta(m/\tau\sigma)$	$\zeta_0(m/\tau\sigma)$	$a(\sigma)$	$\zeta_0(m/\tau\sigma)$	$a(\sigma)$	χ^2_{kin}	χ^2_{hydro}	χ^2_{comb}
10/40	2.0	10.0	0.8800	0.885±0.02	34.8±1.4	109	58.9	259	178	0.0009	0.0059	0.0006
10/40	3.0	3.0	0.8800	0.885±0.02	34.8±1.4	45.5	73.9	168	160	0.0027	0.015	0.0024
10/100	3.0	3.0	0.8830	0.90±0.02	67.2±2.4	52.8	75.7	158	127	0.0061	0.015	0.0023

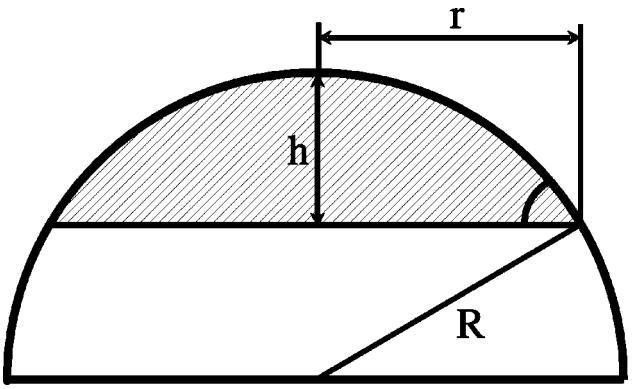

FIG. 3. Diagram of the cylindrical cap.

$$T\sum_w = L\,\eta\dot{r}(t)^2(r(t)-a)/h', \tag{14}$$

where the parameter a has the same meaning as in Ref. [3]; it is a minimum radius cutoff applied to avoid the singularity in the velocity at the z axis. Note that the logarithmic dependence of $T\Sigma_w$ on $r(t)$ for the case of a spreading sphere [3] becomes a linear dependence for the case of a spreading cylinder. Since the rectangular box and the cylindrical cap have the same volume, we can rewrite Eq. (14) in terms of the cylinder dimensions

$$T\sum_w = 2L\,\eta\dot{r}(t)^2\frac{\sin^2\theta(r(t)-a)}{r(t)(\theta-\sin\theta\cos\theta)}. \tag{15}$$

For the spherical geometry, the hydrodynamic dissipation term has been derived previously [3]

$$T\sum_w = 6\pi r(t)\,\eta\phi(\theta(t))\dot{r}(t)^2\ln[r(t)/a], \tag{16}$$

where $\phi(\theta(t))$ is defined as

$$\phi(\theta(t)) = \frac{[1+\cos\theta(t)]\sin\theta(t)}{[1-\cos\theta(t)][2+\cos\theta(t)]}. \tag{17}$$

We construct a combined kinetic and hydrodynamic model in a manner analogous to de Ruijter *et al.* by combining Eqs. (8)–(11) and (15)

$$\dot{r}(t) = \frac{\gamma}{\frac{\zeta_0}{2}+\frac{2\eta(r(t)-a)\sin^2\theta}{r(t)(\theta-\sin\theta\cos\theta)}}\left(\frac{\theta}{\sin\theta}-\frac{\theta_0}{\sin\theta_0}\right). \tag{18}$$

Rewriting this in terms of the contact angle θ using Eq. (5) gives

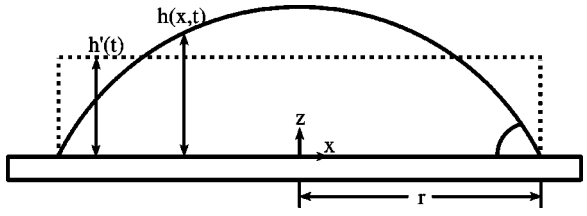

FIG. 4. Rectangular representation of the cylindrical cap.

$$\frac{d\theta}{dt} = \left(\frac{\theta-\sin\theta\cos\theta}{A}\right)^{1/2}\left(\cos\theta - \frac{\sin^3\theta}{\theta-\sin\theta\cos\theta}\right)^{-1}\frac{\gamma\left(\frac{\theta}{\sin\theta}-\frac{\theta_0}{\sin\theta_0}\right)}{\frac{\zeta_0}{2}+\frac{2\eta(r(t)-a)\sin^2\theta}{r(t)(\theta-\sin\theta\cos\theta)}}. \tag{19}$$

This can be compared to the analogous expressions for a spherical droplet [2,3]

$$\dot{r}(t) = \frac{\gamma(\cos\theta_0-\cos\theta)}{\zeta_0+6\eta\phi[\theta(t)]\ln\left(\frac{r(t)}{a}\right)}, \tag{20}$$

$$\frac{d\theta}{dt} = -\left(\frac{\pi}{3V}\right)^{1/3}\frac{(2-3\cos\theta+\cos^3\theta)^{4/3}}{(1-\cos\theta)^2} \times\frac{\gamma(\cos\theta_0-\cos\theta)}{\zeta_0+6\eta\phi[\theta(t)]\ln\left(\frac{r(t)}{a}\right)}. \tag{21}$$

The kinetic model is obtained by setting $\eta=0$ in Eqs. (18)–(21), and the hydrodynamic model is obtained by setting $\zeta_0=0$. For the kinetic model, the asymptotic solutions of Eqs. (18) and (19) give

$$\theta(t) \sim (2A)^{1/5}\left(\frac{5\gamma t}{6\zeta_0}\right)^{-2/5}, \tag{22}$$

$$r(t) \sim 2(2A)^{2/5}\left(\frac{5\gamma t}{6\zeta_0}\right)^{1/5}, \tag{23}$$

as compared to $\theta(t)\sim t^{-3/7}$ and $r(t)\sim t^{-1/7}$ for the spherical geometry. Similarly, the asymptotic solutions for the hydrodynamic model give

$$\theta(t) \sim (2A)^{1/7}\left(\frac{7\gamma t}{48\eta}\right)^{-2/7}, \tag{24}$$

$$r(t) \sim 2(2A)^{3/7}\left(\frac{7\gamma t}{48\eta}\right)^{1/7}, \tag{25}$$

as compared to $\theta(t)\sim t^{-3/10}$ and $r(t)\sim t^{-1/10}$ for the spherical geometry.

IV. RESULTS

A. Comparison to spherical geometry

For wetting droplets, the spreading is characterized by the formation of a precursor foot of monolayer thickness that advances ahead of the bulk of the droplet. The bulk region of the droplet follows the precursor foot at a slower spreading rate. This is demonstrated in Fig. 5, where the contact radius of the foot and bulk regions is plotted as a function of time for both the cylindrical and spherical geometries. These droplets contain 20 000 chains of $N=10$ with a substrate in-

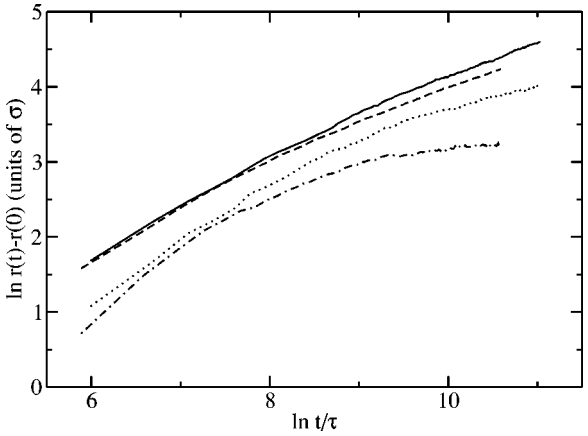

FIG. 5. Radius of the precursor foot for the cylindrical (solid line) and spherical (dashed line) geometries and of the bulk droplet for the cylindrical (dotted line) and spherical (dash-dotted line) geometries. Both cylindrical and spherical droplets consist of 20 000 polymers of length $N=10$. The substrate interaction strength $\varepsilon_w=2.0\ \varepsilon$ is in the fully wetting regime for $N=10$, $\gamma_L^s=10.0\ \tau^{-1}$.

teraction strength $\varepsilon_w=2.0\ \varepsilon$, which is in the fully wetting regime for $N=10$. For the otherwise identical systems, the radii of both regions of the cylindrical droplet increase faster than those for the spherical droplet. This is a consequence of the droplet spreading in one dimension in the cylindrical geometry and two dimensions in the spherical geometry. The precursor foot grows diffusively, $r^2(t)\sim t$, in both cases. We return to further discussion of the time dependence of $r(t)$ in Sec. IV C.

Figure 6 shows the time dependence of the contact angle for the same system. For the contact angle, the cylindrical and spherical geometries show a comparable spreading rate. Since the droplet volume scales as r^3 in the spherical geometry and r^2 in the cylindrical geometry, we favor the cylindrical geometry in order to simulate effectively larger droplets with the same number of monomers.

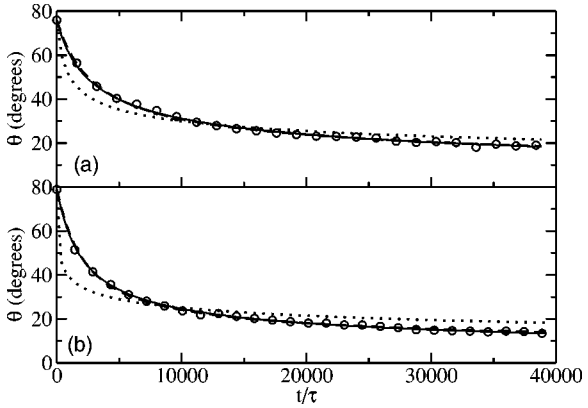

FIG. 6. (a) Fit of the kinetic (solid line), hydrodynamic (dotted line), and combined (dashed line) models to the contact angle data for the cylindrical geometry obtained from MD simulation (◦). (b) Model fits for the equivalent droplet in the spherical geometry. Both cylindrical and spherical droplets consist of 20 000 polymers of length $N=10$. The substrate interaction strength $\varepsilon_w=2.0\ \varepsilon$ is in the fully wetting regime for $N=10$, $\gamma_L^s=10.0\ \tau^{-1}$.

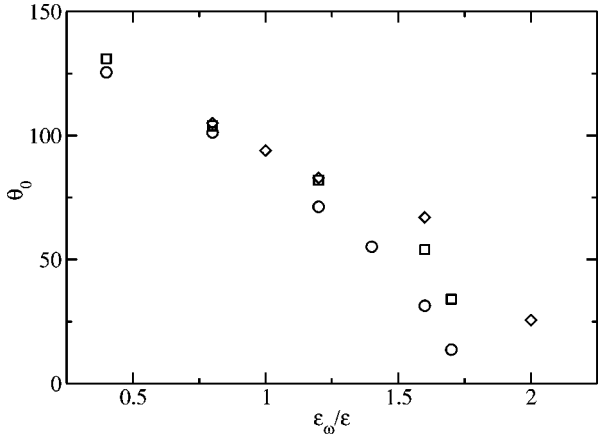

FIG. 7. Equilibrium contact angle as a function of surface interaction strength for polymer droplets composed of $N=10$(◦), $N=40$(□), and $N=100$(◇) monomers per polymer.

Fits to the kinetic, hydrodynamic, and combined models are performed by taking initial guess values for the independent parameters and integrating the expression for $d\theta/dt$ defined in Eqs. (19) and (21) for the cylindrical and spherical droplets, respectively. As these data are in the completely wetting regime, the equilibrium contact angle is fixed at $\theta_0=0°$. The integration uses the fourth-order Runge-Kutta method to generate a set of data, $\theta_{calc}(t)$. The parameters are varied using the downhill simplex method [42] until the difference between the model and simulation data, $|\theta_{calc}(t)-\theta(t)|/\theta(t)$, is minimized. The error reported for each model is calculated as

$$\chi^2=\frac{1}{\mathcal{N}}\sum_{i=1}^{\mathcal{N}}\frac{|\theta_{calc}(t)-\theta(t)|^2}{\theta(t)}, \tag{26}$$

where $\mathcal{N}$ is the number of data points in each set of data.

For the data shown in Fig. 6, the hydrodynamic model provides a more accurate, though still only approximate, fit to the data in the cylindrical geometry. The hydrodynamic cutoff $a\simeq 38.1\ \sigma$ for the spherical geometry and $25.3\ \sigma$ for the cylindrical geometry, indicating stronger hydrodynamic dissipation in the cylindrical geometry. For comparison, the friction coefficients obtained from the kinetic model $\zeta_0=56.3\ m/\tau\sigma$ for the spherical geometry and $56.4\ m/\tau\sigma$ for the cylindrical geometry are in excellent agreement.

B. Chain length dependence

The equilibrium contact angles for nonwetting droplets are plotted as a function of the surface interaction strength in Fig. 7. The variation of the surface tension with chain length, shown in Fig. 1, causes a shift in the wetting transition in terms of the surface interaction strength. The contact angles for the $N=10$ and $N=40$ droplets are taken from earlier work [8] on spherical droplets. The droplets are large enough to eliminate any equilibrium contact angle dependence on the droplet size [8]. Contact angles for the $N=100$ droplets are from simulations containing 355 000 total monomers. Although the chain length dependence is weak for small ε_w, the

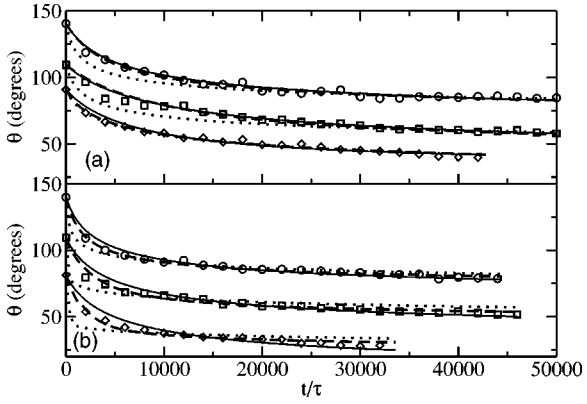

FIG. 8. (a) Fit of the kinetic (solid line), hydrodynamic (dotted line), and combined (dashed line) models to the contact angle data for the cylindrical geometry obtained from MD simulation for $N=10(\circ)$, $N=40(\square)$, and $N=100(\diamond)$ droplets for $\varepsilon_w=2.0\,\varepsilon$, $\gamma_L^s=10.0\,\tau^{-1}$. (b) Same as above with $\varepsilon_w=3.0\,\varepsilon$, $\gamma_L^s=3.0\,\tau^{-1}$. For clarity, the $N=10$ and $N=40$ data sets have been shifted upward 60° and 30°, respectively.

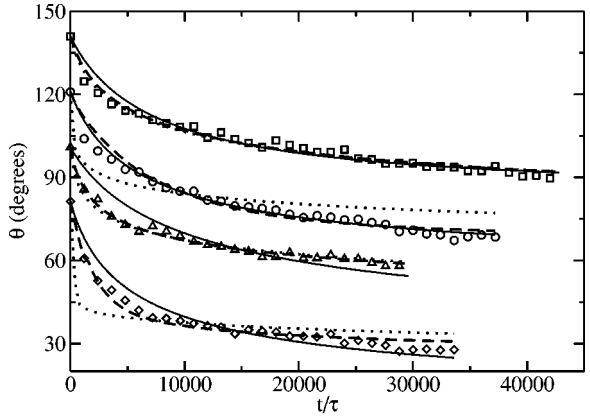

FIG. 9. Fit of the kinetic (solid line), hydrodynamic (dotted line), and combined (dashed line) models to the contact angle data for the cylindrical geometry obtained from MD simulation for $N=100$ with $\varepsilon_w=2.0\,\varepsilon$, $\gamma_L^s=10.0\,\tau^{-1}(\circ)$, $\varepsilon_w=2.0\,\varepsilon$, $\gamma_L^s=3.0\,\tau^{-1}(\square)$, $\varepsilon_w=3.0\,\varepsilon$, $\gamma_L^s=10.0\,\tau^{-1}(\triangle)$, and $\varepsilon_w=3.0\,\varepsilon$, $\gamma_L^s=3.0\,\tau^{-1}(\diamond)$. For clarity, the first three data sets have been shifted upward by 60°, 40°, and 20°, respectively.

wetting transition is shifted to higher ε_w for larger chain lengths due to the increase in the liquid vapor surface tension. The transition occurs near $\varepsilon_w^c \simeq 1.75\,\varepsilon$ for $N=10$ droplets and increases to about $\varepsilon_w^c \simeq 2.25\,\varepsilon$ for $N=100$ droplets. Hence, results shown for $\varepsilon_w=3.0\,\varepsilon$ are in the completely wetting regime for all chain lengths, while those for $\varepsilon_w=2.0\,\varepsilon$ are in the completely wetting regime only for $N=10$ and $N=40$. From Fig. 7, the equilibrium contact angle for $N=100$, $\varepsilon_w=2.0\,\varepsilon$ is $\theta_0 \simeq 26°$. The equilibrium contact angle extracted from the kinetic model fit for this droplet is $\theta_0 \simeq 28°$. For droplets in the completely wetting regime, the models are fit using an equilibrium contact angle fixed at $\theta_0=0°$.

The fits to the simulation data for various chain lengths for $\varepsilon_w=2.0\,\varepsilon$ and $\gamma_L^s=10.0\,\tau^{-1}$ are shown in Fig. 8(a). Figure 8(b) shows results for $\varepsilon_w=3.0\,\varepsilon$ and $\gamma_L^s=3.0\,\tau^{-1}$. The fitting parameters and χ^2 values for all of these droplets are listed in Table I. Overall, the combined model produces the best fits to the data, primarily due to the fact that it has two fitting parameters while the other two models each have one. The kinetic model also fits the data quite well in most cases, which suggests that the combined model overspecifies the droplet spreading behavior for these cases. This is reinforced by the fact that the parameters extracted from the combined model do not correspond well with the physical system. In most cases, the hydrodynamic cutoff a obtained from the combined model is larger than the droplet radius and the friction coefficient is larger than that obtained from the kinetic model. Previously [8], the single-chain diffusion constant was obtained from simulations of polymer melts and the friction coefficient was extracted using the Rouse model via $D=k_BT/mN\zeta_R$. As for the spherical droplets, the friction coefficient ζ_0 obtained from the kinetic model was consistently larger than ζ_R for all cases.

Although the hydrodynamic model performs better for the cylindrical geometry than for the spherical geometry, and gives values for a that are less than the droplet radius in every case, it still provides the poorest fit to the data of the three models. As seen from Fig. 8, the best fit to the hydrodynamic model is for the system with the highest viscosity, $N=100$. To explore this point in greater detail, we ran two additional systems, $\varepsilon_w=2.0\,\varepsilon$ with $\gamma_L^s=3.0\,\tau^{-1}$ and $\varepsilon_w=3.0\,\varepsilon$ with $\gamma_L^s=10.0\,\tau^{-1}$, for $N=100$. The comparison of the fits of the three models to all of the $N=100$ systems is shown in Fig. 9. Only for the droplets with the strongest surface dissipation, $\gamma_L^s=10.0\,\tau^{-1}$, does the hydrodynamic model fit the data very well. The hydrodynamic model fit is very poor for $\gamma_L^s=3.0\,\tau^{-1}$ regardless of the equilibrium contact angle. The strong surface dissipation slows the surface adsorption rate allowing the hydrodynamic behavior to develop in the bulk region of the droplet. On an atomic substrate, this is equivalent to increasing the surface corrugation. The combined model gives fitting parameters that are comparable to both the kinetic and hydrodynamic models only for the two cases where hydrodynamics is important. It should be mentioned that the parameters obtained from the combined model are more sensitive to the input parameters for the $N=100$, $\gamma_L^s=10.0\,\tau^{-1}$ systems. For these two systems, a 10% change in the viscosity results in a 60% change in ζ_0 and a 15% change in a for the combined model. For the other systems, a 10% change in the viscosity results in a 7% change in ζ_0 and a 1% change in a on average. The kinetic model fits the data better for $\varepsilon_w=2.0\,\varepsilon$ than $\varepsilon_w=3.0\,\varepsilon$, presumably because the driving force is smaller since the initial droplet is closer to its final equilibrium contact angle. However, unlike the combined model, the friction coefficients for these two droplets are consistent with those for the other droplets, so we consider the fit parameters to be accurate.

C. Binary droplets

For binary droplets, the behavior is complicated by the interdiffusion of the two components. As the droplet spreads, the component with the smaller surface tension gradually diffuses to the droplet surface. This is evident in the profiles

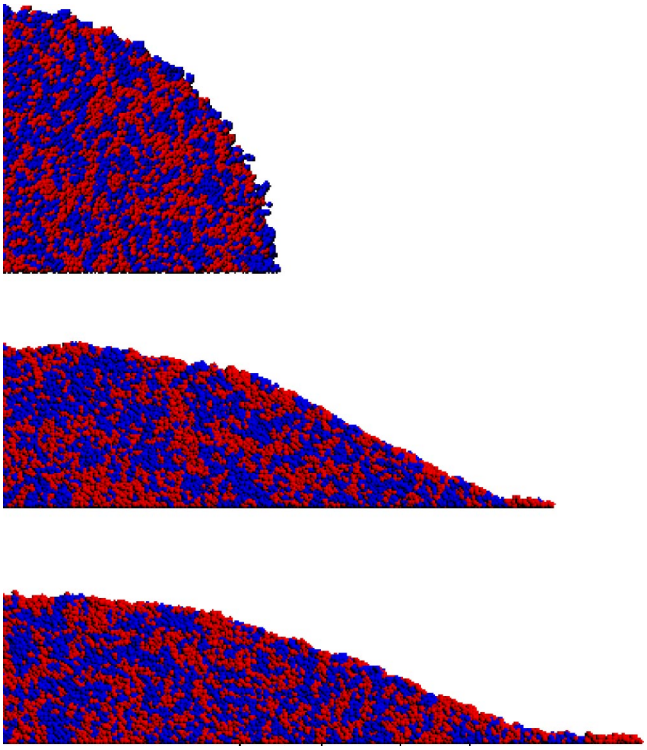

FIG. 10. (Color online) Snapshots of the spreading binary droplet containing 352 000 monomers of a mixture of $N=10$ and $N=40$ polymers. The images are taken from time $t=0$ (top), $t=40\,000\ \tau$ (middle), and $t=80\,000\ \tau$ (bottom). Monomers from $N=10$ chains are shown in red and monomers from $N=40$ chains are shown in blue. $\varepsilon_w=2.0\ \varepsilon$, $\gamma_L^s=10.0\ \tau^{-1}$.

of the binary droplet shown in Fig. 10. The droplet, composed of an initial equimolar mixture of monomers belonging to chains of length $N=10$ and $N=40$, is on a surface with $\varepsilon_w=2.0\ \varepsilon$. Here, the precursor foot pulls ahead of the bulk region as the droplet spontaneously wets the surface. The composition of the precursor foot shows a slight enrichment of the $N=10$ chains, ranging from 59% to 63% in the three frames shown. For $\varepsilon_w=3.0\ \varepsilon$, no segregation in the precursor foot is observed. This can be understood in terms of the relative distance from the wetting transition for each of the components. As shown in Fig. 7, $N=40$ is quite close to the wetting transition for $\varepsilon_w=2.0\ \varepsilon$ and has a significantly slower spreading rate than $N=10$. However, for $\varepsilon_w=3.0\ \varepsilon$, both $N=40$ and $N=10$ are far from the wetting transition and both have fast spreading rates.

Figure 11 shows the dynamics of the contact radius of the precursor foot and the bulk droplet for an equal monomer mole fraction mixture of polymers of chain length $N=10$ and 40 as well as a mixture of $N=10$ and 100 for $\varepsilon_w=3.0\ \varepsilon$ and $\gamma_L^s=3.0\ \tau^{-1}$. Also shown are the contact radius dynamics for the corresponding single-component droplets. In general, the spreading rate of the blend falls between that of the two pure droplets. For either the foot or the bulk, it does not appear that the dynamics of the blend is being dominated by either the $N=10$ or $N=40$ polymers in the 10/40 mixture. Similar results are found for $\varepsilon_w=2.0\ \varepsilon$ and $\gamma_L^s=10.0\ \tau^{-1}$. This is in agreement with earlier simulations [31,34] of blends of chain

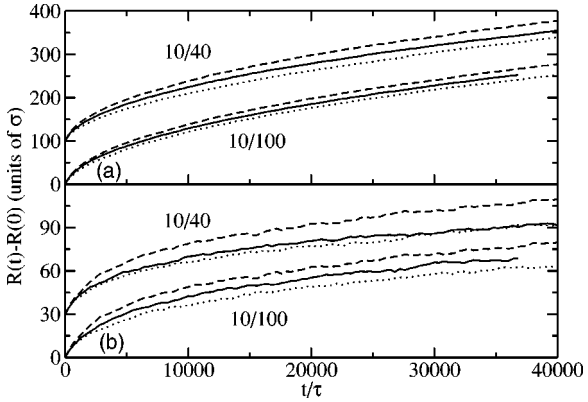

FIG. 11. Spreading rate of (a) the precursor foot and (b) bulk droplet radius for a 352 000 monomer mixture of $N=10$ and $N=100$ polymers (curves shifted upward) and a mixture of $N=10$ and $N=40$ polymers (lower curves) compared to homogeneous polymer droplets of the same size. The curves correspond to $N=10$ (dashed line), $N=40$ or $N=100$ (dotted line), and the 10/40 or 10/100 mixture (solid line). $\varepsilon_w=3.0\ \varepsilon$, $\gamma_L^s=3.0\ \tau^{-1}$.

length $N=8$ and $N=16$ where no significant chain length effects are observed.

For the 10/100 mixture, both components are in the completely wetting regime at $\varepsilon_w=3.0\ \varepsilon$. Here, the contact radius of the bulk region follows the behavior of the $N=100$ droplet more closely than the $N=10$ droplet. This indicates that the spreading of the bulk region of the droplet is limited by the diffusion rate of the larger component. The spreading rate of the foot is nearly equal to the average spreading rate of the two pure components, and the precursor foot composition is about 50% short chain monomers, the same as in the bulk. As found for the 10/40 blend; there is no measurable segregation for the more energetic surface. The case where one component wets the surface and the other does not will be examined in more detail in a future paper where we also study the effect of varying ε_w for two components with the same chain length.

The three spreading models are fit to the contact angle data for a blend of $N=10$ and $N=40$ polymers and for a blend of $N=10$ and $N=100$ polymers. The fitting parameters and associated errors are given in Table II. In every case, ζ_0 from the kinetic model is between that of the corresponding pure component systems. The hydrodynamic model gives a value for a that agrees very well with the pure component system of the larger chain length. The 10/100 mixture is fit much better by the combined model than by either the kinetic or hydrodynamic models, possibly due to a mixture of slow and fast dynamics from the two chain lengths.

V. VELOCITY DISTRIBUTION

To analyze the droplet spreading dynamics in greater detail, we consider the velocity distribution inside the droplet and along the precursor foot. The velocity at a given position in the droplet is obtained by generating a histogram of the instantaneous velocities of the monomers. To eliminate the random fluctuations of the atomic velocities, we average 500

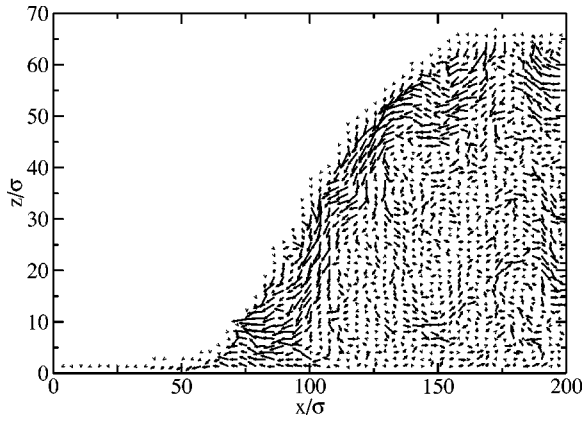

FIG. 12. Instantaneous velocity distribution of a homogeneous droplet after 6000 τ. $N=40$, $\varepsilon_w=3.0\ \varepsilon$, $\gamma_L^s=3.0\ \tau^{-1}$.

such histograms over a period of 50 τ. After generating the averaged histogram, bins containing less than 50 monomers are manually removed. Otherwise, these nearly empty bins would create the illusion of more flow at the surface than is actually present.

The instantaneous velocity of a homogeneous droplet composed of $N=40$ polymers is shown in Fig. 12. The region near the edge of the droplet has the highest velocity, while the monomers at the center of the droplet and near the substrate but not near the edge are almost stationary. This is in sharp contrast to previously published velocity fields of spreading droplets [9,10], which show most of the monomers in the droplet moving at the same speed. In these previous cases, the droplets started as equilibrated spheres placed just above the substrate, having a contact angle of 180°. This has been shown to significantly alter the spreading dynamics of the droplet even well after it adopts a hemispherical shape [8], since the transition from a sphere to a hemisphere imparts a significant amount of momentum. By starting with the droplet equilibrated at a contact angle of less than 90°, we are able to focus on the dynamics induced by the surface tension driving force and not by the momentum gained by the droplet coming into contact with the surface.

The velocity distribution of each component of an equimolar blend of $N=10$ and $N=100$ polymers is shown in Fig. 13. Instead of averaging the instantaneous velocity over a short period, the velocity is calculated from the difference

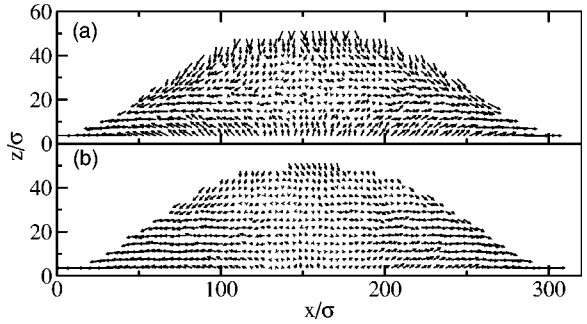

FIG. 13. (a) Velocity distribution of $N=10$ polymers in a 10/100 binary droplet after 20 000 τ. (b) Velocity distribution of $N=100$ polymers in the same droplet. $\varepsilon_w=3.0\ \varepsilon$, $\gamma_L^s=3.0\ \tau^{-1}$.

in monomer positions at 20 000 τ and 40 000 τ. This more clearly demonstrates the slight differences in spreading behavior for the two chain lengths. Figure 13 shows that the shorter chains move more rapidly than the longer chains, but generally exhibit the same behavior. The shorter chains that are buried in the droplet near the substrate show a strong tendency to move away from the substrate, whereas the longer chains show no such tendency even though the shorter chains are farther from the nonwetting transition than the longer chains. This is possibly due to the ability of the shorter chains to diffuse a detectable amount during the 20 000 τ time period, while the longer chains are considerably slower. Figure 13 also indicates that the radial component of the velocity increases as the distance from the center of the droplet increases. A more detailed analysis of the source material of the precursor foot shows that the radial distance traveled by a polymer depends mostly on the initial radial position of the polymer and not on how near it is to the droplet surface. Although the highest velocities are found at the droplet surface, this does not have much influence on the composition of the precursor foot.

VI. CONCLUSIONS

Using molecular dynamics simulation, we study the spreading dynamics of one-and two-component polymer droplets. We apply a cylindrical geometry and demonstrate that the same qualitative spreading behavior is observed as in a spherical geometry. We derive spreading models for the cylindrical geometry based on hydrodynamic and kinetic dissipation mechanisms, and show that hydrodynamic effects become relevant at shorter time scales in the cylindrical geometry. We also show that the $r(t)\sim t^{1/10}$ scaling from the hydrodynamic model and the $r(t)\sim t^{1/7}$ scaling from the kinetic model for spherical droplets become $r(t)\sim t^{1/7}$ and $r(t)\sim t^{1/5}$, respectively, in the cylindrical geometry.

Fitting the models to the spreading data of homogeneous droplets shows that the best fit is obtained using a combination of the kinetic and hydrodynamic dissipation mechanisms, although the parameters extracted from the fit do not agree well with the physical parameters of the system. The hydrodynamic model fit the data well only for the slowest spreading and highest viscosity ($N=100$) case studied, indicating that the kinetic dissipation mechanism may be dominating any hydrodynamic effects for the other cases. By increasing the strength of the surface dissipation, we are able to slow the droplet spreading rate enough for the $N=100$ for hydrodynamic dissipation to be significant.

Compared to homogeneous droplets, the spreading of binary droplets is characterized by the difference in surface tension, viscosity, and interaction strength between the two components and with the substrate. In the binary droplet at equilibrium, the fraction of shorter chains, which have a lower surface tension, is higher at the droplet surface. However, the interdiffusion rate is much slower than the spreading rate for the droplets presented here. As a result, no enrichment of the lower surface tension component is observed either at the droplet surface or in the precursor foot when both components wet the surface. In the case that the differ-

ence in viscosity between the two components is large, the spreading rate of the bulk region is limited by the spreading rate of the more viscous component. Otherwise, the spreading rate is roughly equal to the average rate of the two components. The single binary system for which the combined model performed noticeably better than either the kinetic or hydrodynamic models was the mixture of chain lengths $N=10$ and $N=100$, possibly due to the combination of fast dynamics from $N=10$ chains and slow dynamics from $N=100$ chains.

By starting with droplets that have a contact angle $\theta=90°$ and not with spherical droplets above the substrate, we are able to focus on the dynamics induced by the driving forces of droplet spreading and not by the momentum gained by coming into contact with the substrate. The instantaneous velocity distribution of the spreading droplet shows that spreading occurs by the motion of the droplet surface while the interior of the droplet is almost stationary. For a droplet composed of an equimolar mixture of short-chain and long-chain polymers, we find that the shorter chains move more rapidly than the longer ones near the surface of the droplet. From the droplet surface, they move downward to the precursor foot and then outward along the substrate.

Future work will include studying the effects of the interaction strength between the two components and the effects of patterned surfaces.

ACKNOWLEDGMENTS

Sandia is a multiprogram laboratory operated by Sandia Corporation, a Lockheed Martin Company, for the United States Department of Energy's National Nuclear Security Administration under Contract No. DE-AC04-94AL85000.

[1] P. G. de Gennes, Rev. Mod. Phys. **57**, 827 (1985).
[2] M. J. de Ruijter, M. Charlot, M. Voué, and J. De Coninck, Langmuir **16**, 2363 (2000).
[3] M. J. de Ruijter, J. De Coninck, and G. Oshanin, Langmuir **15**, 2209 (1999).
[4] R. G. Cox, J. Fluid Mech. **168**, 169 (1986).
[5] C. Huh and L. E. Scriven, J. Colloid Interface Sci. **35**, 85 (1971).
[6] L. H. Tanner, J. Phys. D **12**, 1473 (1979).
[7] O. V. Voinov, Fluid Dyn. **11**, 714 (1976).
[8] D. R. Heine, G. S. Grest, and E. B. Webb III, Phys. Rev. E **68**, 061603 (2003).
[9] T. D. Blake, A. Clarke, J. De Coninck, M. de Ruijter, and M. Voué, Colloids Surf., A **149**, 123 (1999).
[10] M. J. de Ruijter, T. D. Blake, and J. De Coninck, Langmuir **15**, 7836 (1999).
[11] M. de Ruijter, T. D. Blake, A. Clarke, and J. De Coninck, J. Pet. Sci. Eng. **24**, 189 (1999).
[12] J. De Coninck, U. D'Ortona, J. Koplik, and J. R. Banavar, Phys. Rev. Lett. **74**, 928 (1995).
[13] U. D'Ortona, J. De Coninck, J. Koplik, and J. R. Banavar, Phys. Rev. E **53**, 562 (1996).
[14] J. Yang, J. Koplik, and J. R. Banavar, Phys. Rev. Lett. **67**, 3539 (1991).
[15] J. Yang, J. Koplik, and J. R. Banavar, Phys. Rev. A **46**, 7738 (1992).
[16] J. A. Nieminen, D. B. Abraham, M. Karttunen, and K. Kaski, Phys. Rev. Lett. **69**, 124 (1992).
[17] P. van Remoortere, J. E. Metrz, L. E. Scriven, and H. T. David, J. Chem. Phys. **110**, 2621 (1999).
[18] J. B. Freund, Phys. Fluids **15**, L33 (2003).
[19] F. Brochard-Wyart and P. G. de Gennes, Adv. Colloid Interface Sci. **39**, 1 (1992).
[20] T. D. Blake, *Wettability* (Marcel Dekker, New York, 1993).
[21] C. Redon, D. Ausserre, and F. Rondelez, Macromolecules **25**, 5965 (1992).
[22] U. Steiner, J. Klein, E. Eiser, A. Budkowski, and L. J. Fetters, Science **258**, 1126 (1992).
[23] R. Fondecave and F. Brochard-Wyart, Europhys. Lett. **37**, 115 (1997).
[24] F. Brochard-Wyart, R. Fondecave, and M. Boudoussier, Int. J. Eng. Sci. **38**, 1033 (2000).
[25] A. I. Posazhennikova, J. O. Indekeu, D. Ross, D. Bonn, and J. Meunier, J. Stat. Phys. **110**, 611 (2003).
[26] M. C. Yeh and L. J. Chen, J. Chem. Phys. **118**, 8331 (2003).
[27] J. A. Nieminen and T. Ala-Nissila, Europhys. Lett. **25**, 593 (1994).
[28] J. A. Nieminen and T. Ala-Nissila, Phys. Rev. E **49**, 4228 (1994).
[29] A. Milchev and K. Binder, J. Chem. Phys. **116**, 7691 (2002).
[30] J. Yaneva, A. Milchev, and K. Binder, Macromol. Theory Simul. **12**, 573 (2003).
[31] M. Voué, S. Rovillard, J. De Coninck, M. P. Valignat, and A. M. Cazabat, Langmuir **16**, 1428 (2000).
[32] S. Gladstone, K. J. Laidler, and H. J. Eyring, *The Theory of Rate Processes* (McGraw-Hill, New York, 1941).
[33] T. D. Blake, Ph.D. thesis, University of Bristol, 1968.
[34] T. D. Blake and J. M. Haynes, J. Colloid Interface Sci. **30**, 421 (1969).
[35] A. E. Seaver and J. G. Berg, J. Appl. Polym. Sci. **52**, 431 (1994).
[36] K. Kremer and G. S. Grest, J. Chem. Phys. **92**, 5057 (1990).
[37] O. M. Braun and M. Peyrard, Phys. Rev. E **63**, 046110 (2001).
[38] S. Plimpton, J. Comput. Phys. **117**, 1 (1995).
[39] M. J. P. Nijmeijer, A. F. Bakker, C. Bruin, and J. H. Sikkenk, J. Chem. Phys. **89**, 3789 (1988).
[40] D. G. LeGrand and G. L. Gaines Jr., J. Colloid Interface Sci. **50**, 272 (1975).
[41] M. P. Allen and D. J. Tildesley, *Computer Simlations of Liquids* (Clarendon Press, Oxford, 1987).
[42] W. H. Press, S. A. Teukolsky, W. T. Vetterling, and B. P. Flannery, *Numerical Recipes in C* (Cambridge University Press, Cambridge, 1992).
[43] P. G. de Gennes, *Liquids at Interfaces* (North-Holland, New York, 1990), p. 371.
[44] M. Voué and J. De Coninck, Acta Mater. **48**, 4405 (2000).